Metallogr. Microstruct. Anal. (2012) 1:14–27
DOI 10.1007/s13632-011-0001-9

TECHNICAL ARTICLE

Microstructures for Two-Phase Gamma Titanium Aluminide Fabricated by Electron Beam Melting

Jennifer Hernandez · Lawrence E. Murr · Sara M. Gaytan · Edwin Martinez · Frank Medina · Ryan B. Wicker

Received: 2 November 2011 / Accepted: 16 December 2011 / Published online: 28 February 2012

Abstract Pre-alloyed (Ti-48Al-2Cr-2Nb) powder was used to fabricate solid, fully dense (3.85 g/cm^3) components by electron beam melting (EBM). Foam components with densities from 0.33 to 0.46 g/cm^3 were also fabricated by EBM. Both the solid and the foam component microstructures were characterized by an equiaxed, duplex grain structure (15 μm diameter) containing lamellar α_2 (Ti_3Al)/γ (TiAl) plates ~20 nm. Light optical metallography and transmission electron microscopy illustrated that these microstructures confirmed the $(111)_\gamma/(001)_{\alpha 2}$ duplex orientation relationship. Solid components annealed at 1150 °C at 5 h and 1380 °C at 1 h exhibited a fine-grain (3 μm diameter) duplex structure and a large, equiaxed, fully lamellar grain structure (550 μm diameter), respectively. The lamellar structure consisted mostly of coherent {111} γ (TiAl) twins with a width of ~0.9 μm. These diverse annealed microstructures exhibited residual hardness values similar to the as-fabricated EBM components.

Keywords Two-phase TiAl · Electron beam melting · Metallography and microstructure analysis · Hardness measurements

J. Hernandez (✉) · L. E. Murr · S. M. Gaytan · E. Martinez
Department of Metallurgical and Materials Engineering, University of Texas at El Paso, El Paso, TX 79968, USA
e-mail: jhernandez42@miners.utep.edu

J. Hernandez · L. E. Murr · S. M. Gaytan · E. Martinez · F. Medina · R. B. Wicker
W. M. Keck Center for 3D Innovation, University of Texas at El Paso, El Paso, TX 79968, USA

Introduction

For more than two decades, γ-titanium aluminides (γ-TiAl) have been considered to be novel and practical candidates for automotive engine components, industrial and aviation turbines (especially compressor blades), as well as structural applications in oxidizing environments up to ~700 °C. Above 900 °C both TiO_2 and Al_2O_3 surface corrosion products occur. This is due primarily to attractive properties which include low density ($\rho \sim 3.9$ g/cm^3), high specific strength (σ_γ/ρ), high specific stiffness (E/ρ), and good corrosion/oxidation resistance as noted; where σ_γ and E are the yield strength and Young's modulus, respectively.

As noted in a comprehensive review by Appel and Wagner [1], single-phase γ-TiAl, like many intermetallic phases at room temperature, exhibits poor ductility and fracture toughness while two-phase alloys with compositions in the ($\gamma + \alpha$) two-phase region of the Ti-Al (binary) phase diagram (Fig. 1) can exhibit improved ductility and toughness. Extensive research has been carried out to develop two-phase γ-TiAl-based alloys consisting of γ-TiAl with the ordered face-centred tetragonal $L1_O$ structure ($p4mmm$; $a \cong 0.41$ nm $\cong$ b and essentially, fcc), and α_2-Ti_3Al with the hexagonal DO_{19} structure ($p63/mmc$; $a = 0.58$ nm, $c = 0.46$ nm) [1, 2]. Additions of β-stabilizing elements such as Cr, Nb, W, and Mo can also produce the body-centered cubic β-phase (Fig. 1) which is softer than the γ and α_2 phases at elevated temperature [3]. This may influence creep properties and can create β precipitates at lamellar α_2/γ interfaces.

The γ-TiAl compositions have been difficult to process using pre-alloyed powders in conventional PM processing [4] while investment castings or processing ingots to various mill product forms has also posed problems such as

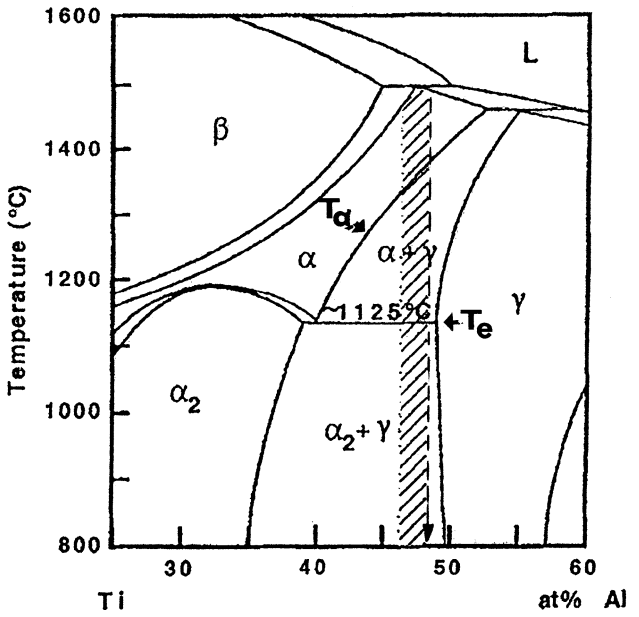

Fig. 1 Central portion of the binary Ti-Al phase diagram. The compositional ranges are shown hatched for two-phase engineering materials. $T_e = 1124$ °C is the eutectoid temperature. Between T_e and T_α (the α transus temperature) duplex microstructures with ranging volume fraction of lamellar grains occurs. Dotted line shows alloy composition for this study

thermal stress-induced cracking, especially at lower temperatures [5]. More recently, Cormier et al. [6] and Murr et al. [7] have demonstrated the fabrication of γ-TiAl prototypes by additive manufacturing using electron beam melting (EBM). In all the processing routes for γ-TiAl, the as-processed microstructure usually assumes some duplex form ($\gamma + \alpha_2$): γ-TiAl lamellae with interspersed α_2-Ti_3Al; often equiaxed lamellar colonies interspersed with γ-TiAl grains containing no lamellae [1, 2]. The lamellar structure is formed when Ti-rich two-phase alloys are hot worked or heat treated in the vicinity of the α transus line (Fig. 1), and displays a plate-like morphology consisting of parallel, thick plates of γ-TiAl, and very fine plates of α_2-Ti_3Al. The orientation relationship between the two phases is well documented to be [1, 8]:

$$(111)\gamma||(000)\alpha_2 \quad \text{and} \quad \langle 1\bar{1}0]\gamma||\langle 11\bar{2}0\rangle\alpha_2,$$

where the (111) plane is parallel to the lamellae (α_2/γ) interfaces.

Unlike nickel-titanium alloys or nickel aluminides, titanium aluminides have not been fabricated in porous or open-cellular structure forms [9, 10]. These forms are ideal in applications where properties must be optimized in relation to the overall system weight and high-temperature applications with severe environments. Novel and complex mesh and foam structures have recently been fabricated for Ti-6Al-4V [11] and Co-base and Ni-base superalloys [12] having relative densities (ρ/ρ_o) as low as 0.075.

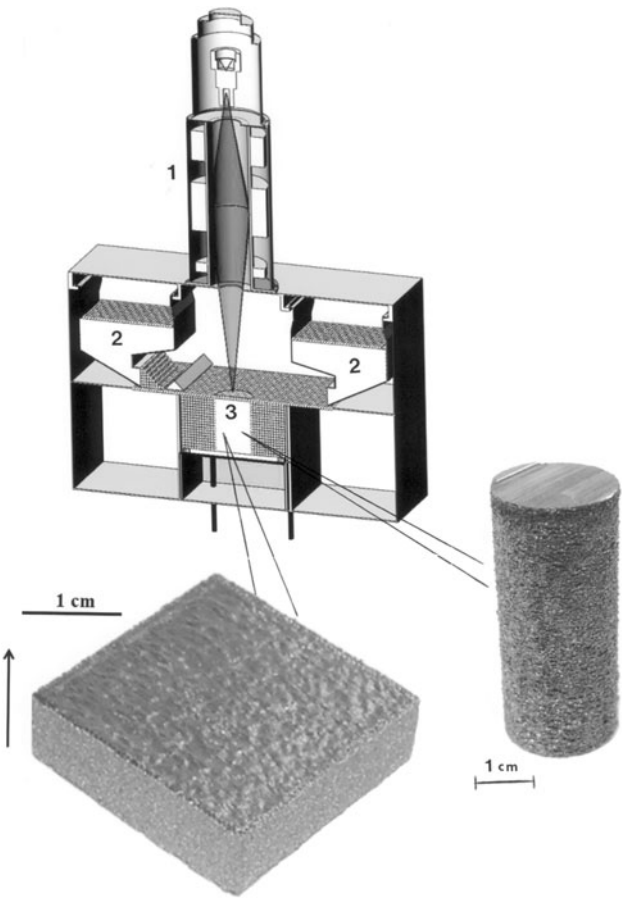

Fig. 2 EBM system schematic and solid component geometries

In this study, we examined the microstructures in fully dense γ-TiAl components fabricated by additive manufacturing (AM) using EBM of pre-alloyed, atomized powder using light optical metallography (LOM) and transmission electron microscopy (TEM). Preliminary open-cellular (foam) components were also fabricated for a range of densities (ρ), and the foam-ligament microstructures also observed by LOM.

Experimental Procedures

Fabrication of Solid Components by EBM

Figure 2 shows a schematic view for the Arcam A2 EBM system and examples of solid component geometries fabricated in this study. The EBM system is composed primarily of an electron optical column (1 in Fig. 2) which generates electrons in a gun with an acceleration potential of 60 kV. Electromagnetic lenses focus the electron beam and scan coils scan the beam selectively across powder layers formed by raking the powder, gravity fed from cassettes shown at (2) in Fig. 2. Selective melting directed

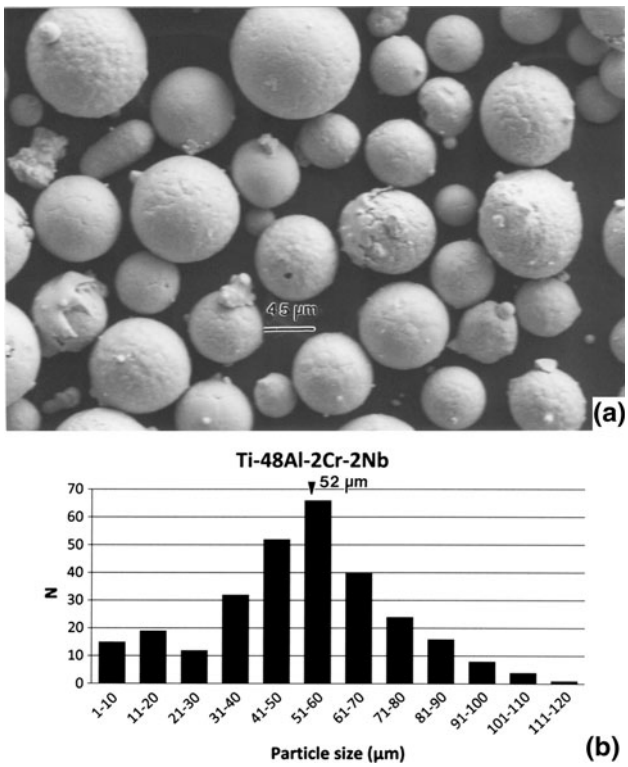

Fig. 3 Pre-alloyed Ti-Al precursor powder (**a**) and powder particle size distribution histogram (**b**). The average powder particle size (including attached satellite particles) is shown to be 52 µm

by a CAD model creates a build layer at (3) in Fig. 2 forming components shown layer-by-layer. Prior to the melt scan the beam is rapidly scanned at higher beam current to pre-heat the raked powder layer in multiple passes, and the final melt scan is accomplished at reduced scan speed and beam current [11]. Figure 3(a) illustrates the rapidly solidified (atomized) pre-alloyed powder having a composition of Ti-48Al-2Cr-2Nb (in atomic percent), while Fig. 3(b) shows the corresponding powder size distribution and average powder particle size.

Foam Component Building Strategy

Stochastic foams of γ-TiAl were fabricated from CAD models developed from CT scans of conventional aluminum foams as discussed in detail elsewhere [11]. This digital layer data was imported into bitmap files representing image or model slices with specific pixel dimensions to create expandable elements for the development of models implicit in Fig. 4. These file-model representations can be altered dimensionally to create cell size or pore size variations as well as ligament dimension variations (particularly thickness), resulting in specific density or porosity variations [11].

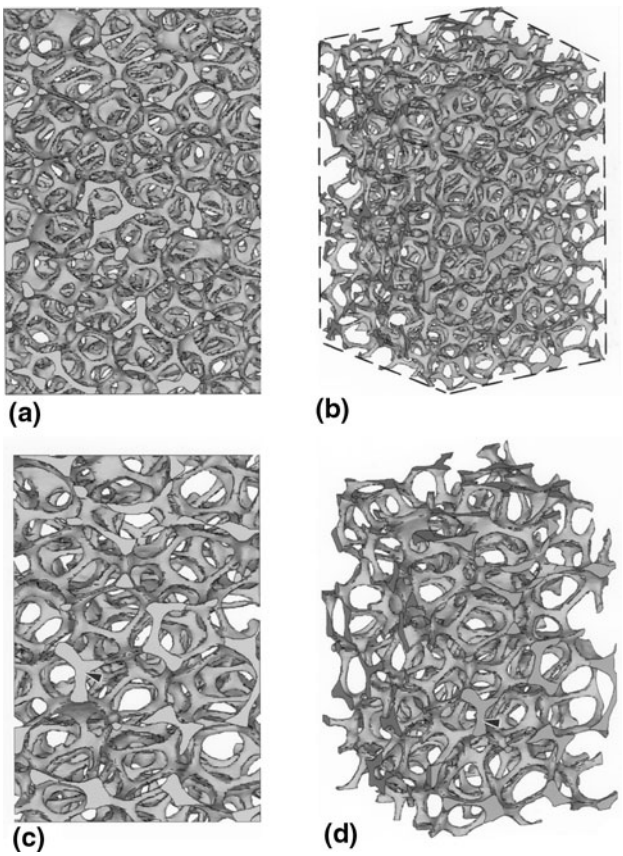

Fig. 4 Stochastic foam model for EBM building of open-cellular γ-TiAl components created from CT-scan data. (**a**) 3D foam model. (**b**) Face view for foam pore and ligament structure

Microstructural and Material Characterization

Microstructures for solid and open-cellular EBM fabricated components were observed by LOM using a digital imaging metallograph. Precursor, pre-alloyed powder microstructures were also examined by embedding in a mounting epoxy and grinding, polishing, and etching to reveal particle interiors. Etching of exposed powder interiors as well as mounted, ground, and polished solid and foam samples utilized a solution consisting of 5 mL HNO_3, 10 mL HF, and 300 mL H_2O. Samples were etched generally for $\sim$1 s and washed in ethanol to remove residual etchant. Samples were also observed in a Hitachi S-8500 field emission scanning electron microscope (SEM) operated at 20 kV, utilizing an EDAX energy dispersive (x-ray) spectrometer (EDS) attachment for elemental analysis. Powder and solid (including foam) specimens were also examined by x-ray diffraction (XRD) using a Bruker AXS-D8 (Discover) XRD system.

Sections were cut from the EBM-fabricated solid components illustrated in Fig. 2 in slices oriented either parallel or perpendicular to the build direction indicated by the

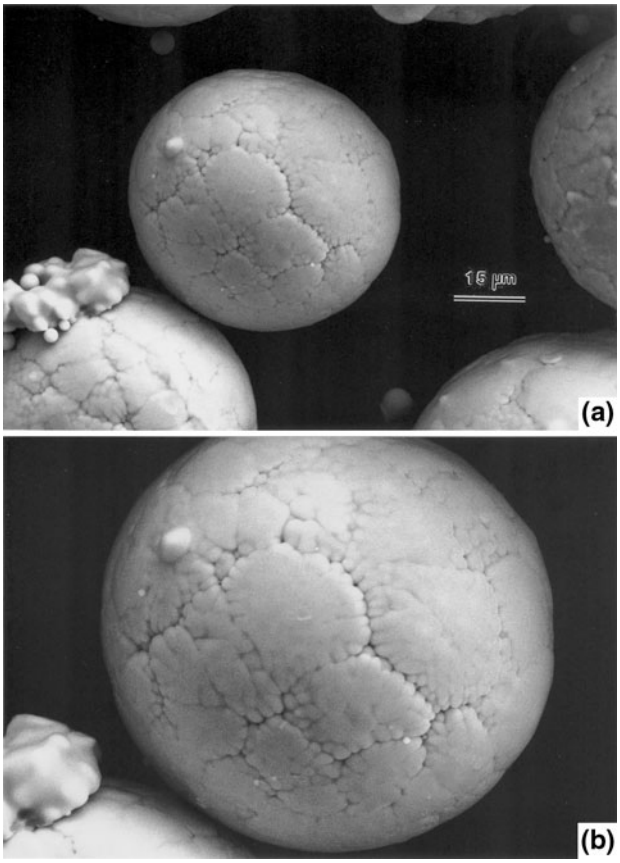

Fig. 5 Magnified views for the precursor Ti-48Al-2Cr-2Nb powder in Fig. 3(a)

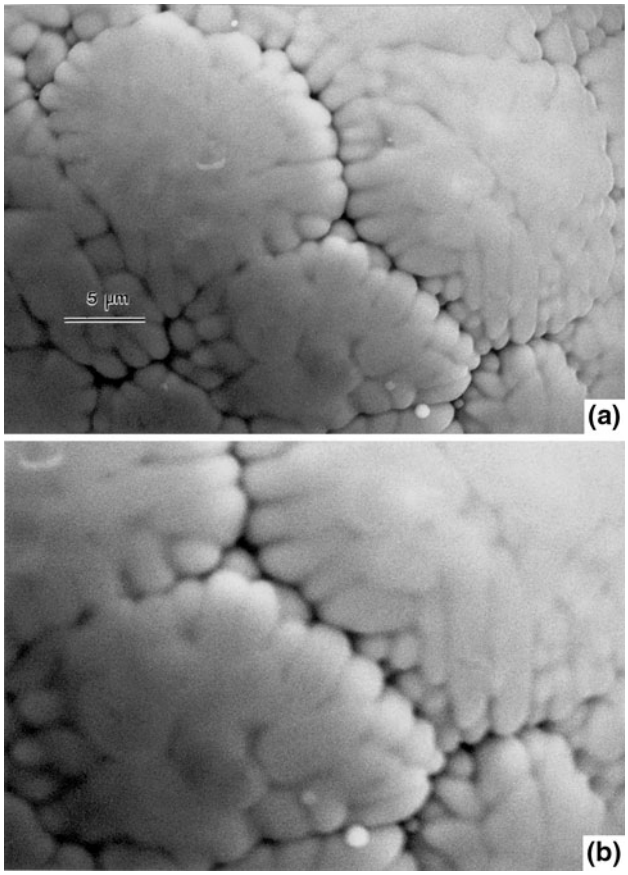

Fig. 6 Magnified views for the powder particle in Fig. 5 showing microdendritic grain structure

arrow at the lower left in Fig. 2. These slices were ground and polished to a thickness of 200 μm and 3 mm discs punched from them. These discs were electropolished from both sides in a dual jet electropolishing unit operated at a polishing current ranging from ~5 to 10 A at ~15 V. The electropolishing solution consisted of 950 mL methanol and 50 mL perchloric acid at −30 °C. The electropolished/electrothinned discs were examined in a Hitachi H-9500 high-resolution TEM operating at 300 kV, fitted with a digital CCD camera and an EDAX elemental analysis (EDS) system.

Residual microindentation (Vickers) hardness for the mounted, polished, and etched powder as well as the solid components (Fig. 2), and foam sample ligaments, was measured using a Struers-Doramin A-300, digital instrumental system; utilizing a 100 gf (1 N) load with a dwell time of 10 s. For solid sections, a minimum of 10 indentations were made following standard steel block calibration. Similar indentations were made for mounted foam ligaments which were at least three indenters wide. This assured microindentation measurements were representative.

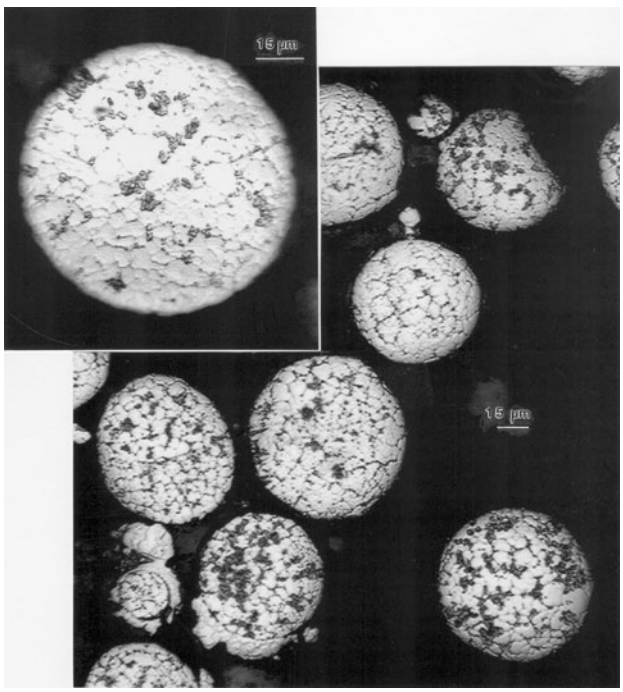

Fig. 7 LOM section views showing internal, equiaxed, dendritic grain structure of the pre-alloyed precursor powder

Results and Discussion

Figures 5 to 7 illustrate the powder microstructure to be an equiaxed, microdendritic (cellular) grain structure ($\sim$2 μm) exhibiting a duplex α_2/γ crystal structure ($\alpha_2/\gamma = 0.5$)

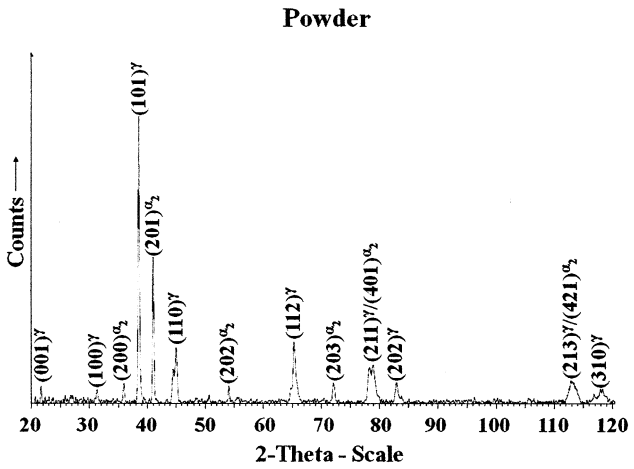

Fig. 8 XRD spectra for the Ti-48Al-2Cr-2Nb precursor powder in Fig. 3(a)

as illustrated in the XRD spectra of Fig. 8. In comparison, Figs. 9 and 10 show 3D composite LOM views of the solid, rectangular, and cylindrical EBM component (Fig. 2) microstructures to consist of a duplex (α_2/γ), equiaxed grain structure ($\sim$15 μm grain size) composed of colony-lamellar substructures, primarily γ-TiAl. The measured density for the solid components averaged 3.85 g/cm^3. XRD spectra corresponding to the horizontal and vertical reference plane section for Figs. 9 and 10 are shown in Figs. 11 and 12, respectively, where $\alpha_{2/\gamma} \cong 0.05$. Figure 13 shows an LOM (lower magnification) view of the vertical plane section corresponding to Fig. 10 (cylindrical component) illustrating etching contrast delineating successive layering, representative of layer thicknesses of $\sim$100 μm.

Figure 14 shows foam prototype components representing a range of densities, indicated. The SEM view in Fig. 15, typical for the ligaments, shows the partially melted/sintered powder particles characterizing the surface structure. Figure 16 shows a typical LOM view of the ligament microstructure which corresponds to those shown in Figs. 9 and 10 for the solid components: exhibiting a generally equiaxed duplex grain structure $\sim$15 μm grain

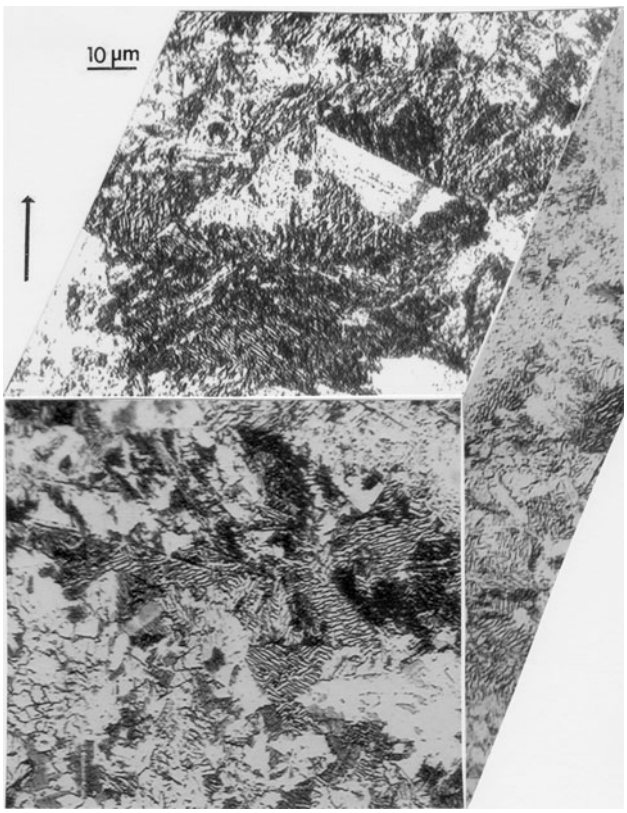

Fig. 9 3D-LOM composite view for dual-phase γ-TiAl microstructure representative of the EBM-fabricated rectangular solid (Fig. 2). The build direction is indicated by the arrow (left)

Fig. 10 3D-LOM composite view for dual-phase γ-TiAl microstructure representative of the EBM-fabricated cylindrical solid (Fig. 2). The build direction is indicated by the arrow (left)

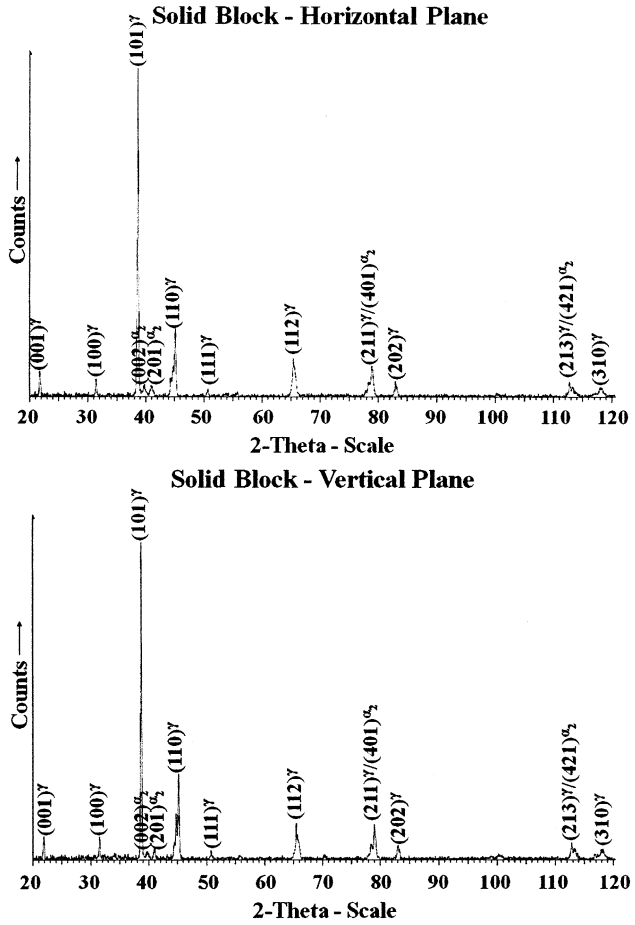

Fig. 11 XRD spectra corresponding to the horizontal and vertical reference planes for a rectangular EBM-fabricated block (represented by Fig. 9)

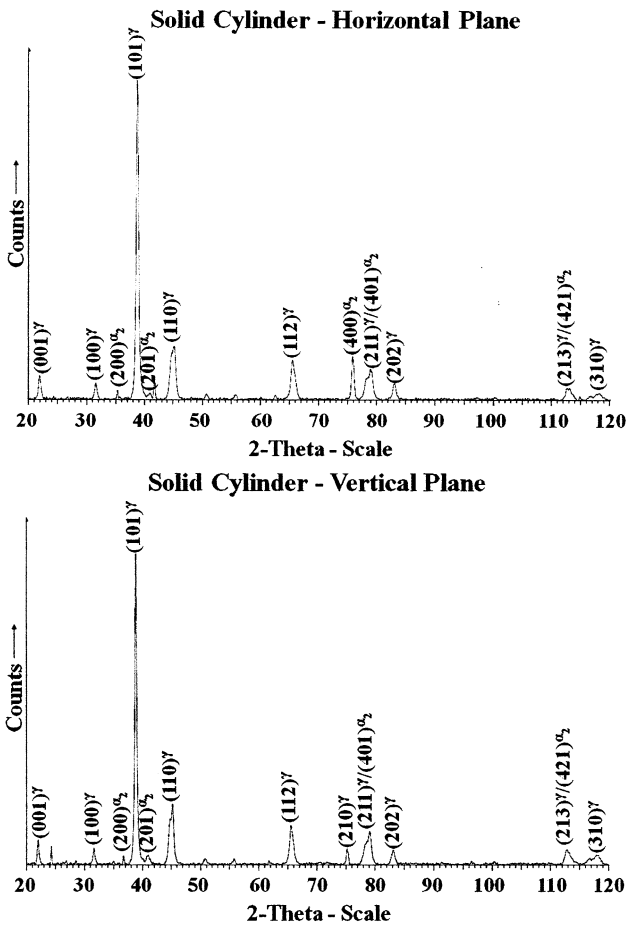

Fig. 12 XRD spectra corresponding to the horizontal and vertical reference planes for a cylindrical EBM-fabricated component (represented by Fig. 10)

diameter. The XRD spectra characteristic of the foam ligaments are shown in Fig. 17. In contrast to the corresponding solid component XRD spectra shown in Figs. 11 and 12, the foam exhibits slightly less α_2 ($\alpha_2/\gamma \leq 0.05$).

Figure 18 compares typical horizontal and vertical reference plane TEM images characterizing microstructures illustrated in the LOM-3D composition in Fig. 9. These images show relatively equiaxed γ-TiAl grains with and without α_2/γ lamellar microstructures. Figures 19 to 21 show the details of the lamellar α_2/γ microstructures in the horizontal reference plane of a rectangular (block) component (Fig. 2) specimen. Figure 19 shows a large, lamellar-containing grain separated from smaller, generally equiaxed γ-TiAl grains. Figure 20 shows the details of the thin α_2 (hcp) coincident plates $(11\bar{1})_\gamma || (0001)\alpha_2)$ which are perpendicular to the (123) fcc (γ-TiAl) surface orientation as indicated in the selected-area electron diffraction (SAED) pattern insert showing γ-TiAl and α_2-Ti_3Al diffraction spots along $[11\bar{1}]_\gamma$ (arrow in Fig. 20 SAED pattern inset); perpendicular to the $(11\bar{1})$ plane which is perpendicular to the (123) surface plane or indicated previously. These α_2 platelets are roughly only 20 nm thick, while in some cases both the α_2 and γ regions have similar thicknesses as illustrated in the bright-field/dark-field (DF) TEM sequence shown in Fig. 21(a) and (b), respectively, where only small γ-TiAl platelets reverse contrast in DF (Fig. 21b).

While the solid, cylindrical EBM components (Fig. 2) exhibited microstructures essentially the same as those shown for comparison in Figs. 9 and 10, and the TEM images illustrated in Figs. 18 to 21, the TEM images shown in Figs. 22 to 25 illustrate similar and related microstructures which characterize the solid components overall. Figure 22 shows a horizontal section view for a cylindrical sample containing some α_2 platelets within the γ-TiAl as well as a relatively high density of dislocation structures. Correspondingly, Fig. 23 illustrates a large array of dislocation dipoles in a similar specimen section. There are strain contrast regions along α_2/γ interfaces to the left in Fig. 23 (arrow). These may be ledge structures

Fig. 13 Low-magnification LOM image showing additive-larger structures in the vertical reference plane for a cylindrical EBM-fabricated component (represented by Fig. 10)

illustrated in previous work of Appel et al. [2]. Figure 24 shows a γ-TiAl grain containing thin α_2 platelets having the same orientation/crystallographic relationships noted for Fig. 20. The arrow in Fig. 24 is identical to the arrow in the SAED pattern inset in Fig. 20, and represents the $[11\bar{1}]$ direction characterizing the arrays of diffraction spots in the SAED pattern inset in Fig. 24. Figure 25, in contrast to Fig. 21, illustrates a bright-field/DF sequence showing contrast reversal for large segments of α_2 platelets, utilizing the operating reflection shown circled in the SAED pattern inset in Fig. 25.

In the conventional processing of titanium aluminides, including ingot metallurgy [13], investment casting [14], and powder metallurgy [15], duplex microstructures following HIP (after investment casting) at temperatures around 1200 °C appear similar to those shown in Figs. 9 and 10 and Fig. 16 for solid and foam components, respectively. Near-γ (globular) microstructures consisting of very fine, equiaxed grains ($\sim$10 μm) have been observed after two-step isothermal forging at 1220 °C, while fully lamellar microstructure occurs with additional heat treatment at 1370 °C/1 h → 900 °C/6 h → 20 °C which produces an equiaxed grain structure with average grain sizes >300 μm [2]. The duplex microstructure yields the highest elongation ($\sim$2%) with poor toughness [1, 16], while the fully lamellar grain structures exhibit

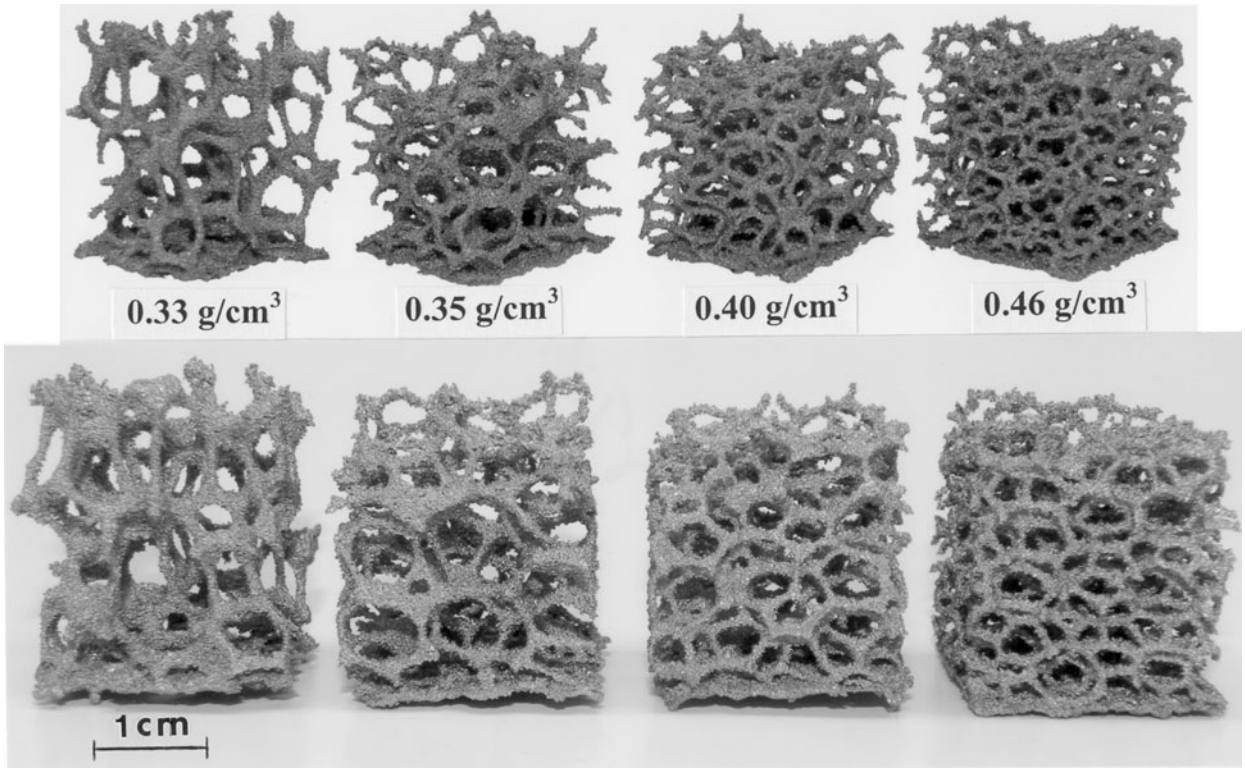

Fig. 14 Ti-48Al-2Cr-2Nb foam prototypes fabricated by EBM. Top row shows edge orientations while bottom row shows face orientations at slight larger magnifications. Measure densities are indicated

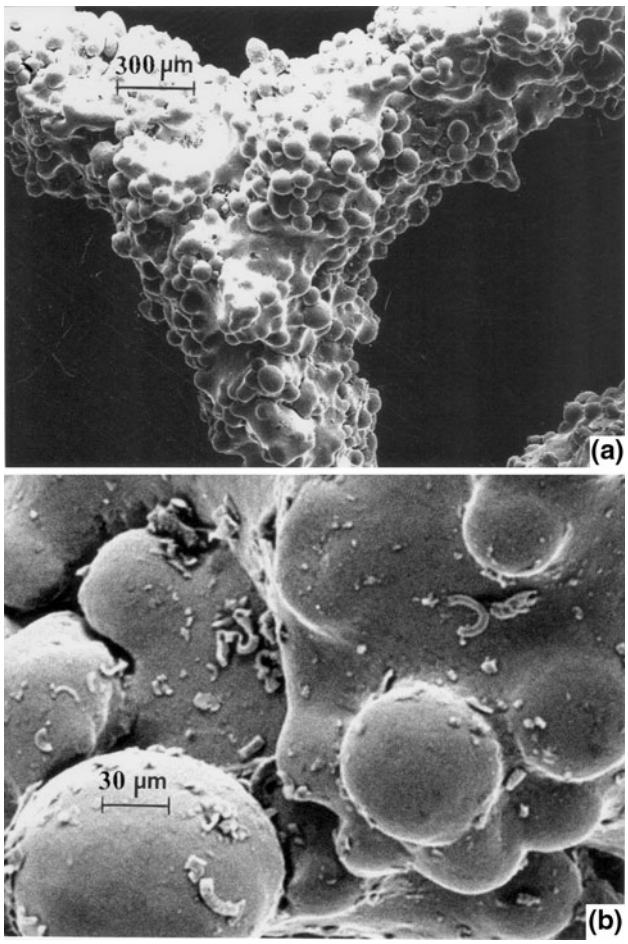

Fig. 15 SEM views for ligament structure of foam sample ($\rho = 0.33$ g/cm^3) showing partially sintered powder particles. (**a**) Low-magnification SEM image. (**b**) High-magnification view showing partially sintered powder particles

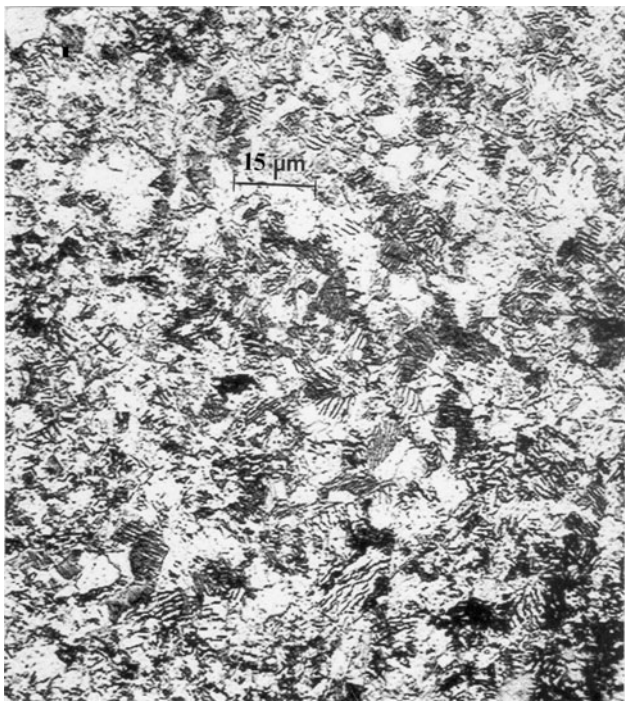

Fig. 16 Foam ligament microstructure: OM image showing duplex (two-phase) structure

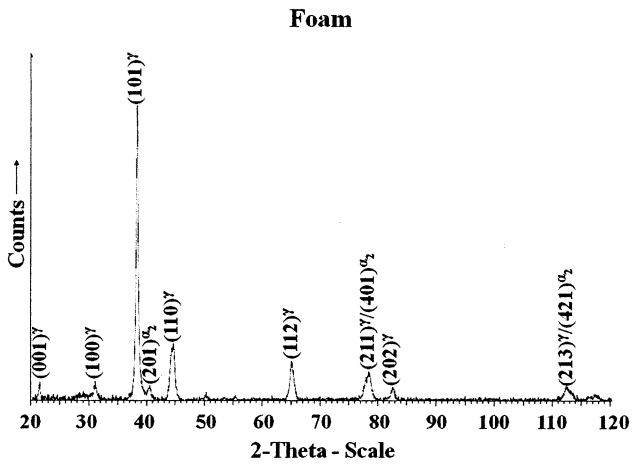

Fig. 17 XRD spectra for the foam components

improved creep strength and fracture toughness, with reduced elongation in contrast to the fine-grain, duplex structures [1, 17].

In this research program, we emulated these contemporary microstructures by annealing the EBM-fabricated, rectangular block specimens shown in Fig. 2 using two schedules: (1) specimens were annealed at 1150 °C for 5 h in purified argon (and furnace cooled); (2) specimens were annealed at 1380 °C for 1 h in argon (and furnace cooled). For schedule (1), a single-step annealing process, equiaxed fine grains ($\sim$3 μm) occurred with some remanent larger-grain, occluded clusters. For schedule (2) or anneal (2), a large equiaxed, fully lamellar grain structure was observed having an average grain size of 550 μm. Figure 26 compares these two anneal schedule microstructures observed by LOM. Figure 27 shows some examples of the Anneal (1) microstructures/substructures observed in the TEM, where in contrast to the TEM images shown in Figs. 18 and 19 for the EBM-fabricated, solid block specimens, there is no corresponding lamellar microstructure, and irregular α_2 platelets are intermixed with γ-TiAl {111} twins. This is particularly notable in Fig. 27(b) which shows a slightly magnified (123)-oriented grain with $(\bar{1}\bar{1}1)$ and $(1\bar{1}1)$ coincident lamellae. Correspondingly, Fig. 28 shows a bright-field/DF TEM sequence showing thin, γ-TiAl $11\bar{1}$ twins intermixed with thin lamellar α_2 (Ti_3Al). The SAED pattern inset shows the $[11\bar{1}]$ direction (arrow) normal to the $(11\bar{1})$ planes which are correspondingly normal to the

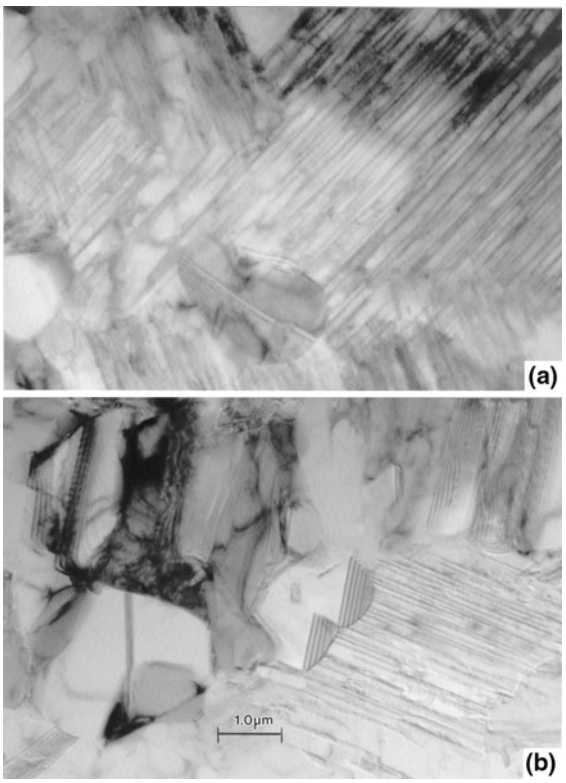

Fig. 18 Comparative TEM images for two-phase microstructures in EBM-fabricated γ-TiAl cylindrical component. (**a**) Horizontal reference plane. (**b**) Vertical reference plane (Fig. 10)

Fig. 19 TEM bright-field image showing lamellar (α_2/γ) filled grain (top) and primarily γ-TiAl grains (bottom)

(123) grain surface. These orientation and crystallographic features emulate those shown previously in Figs. 20 and 21. In contrast to the EBM-fabricated block and cylindrical

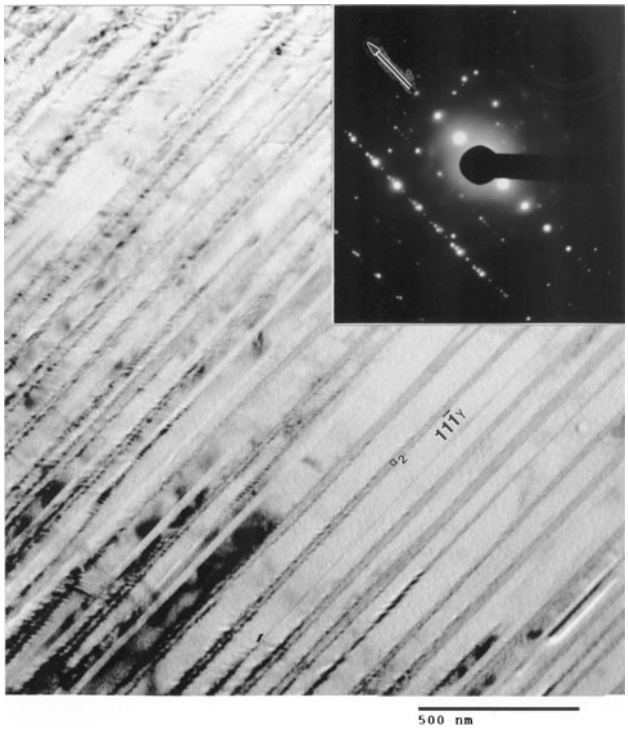

Fig. 20 Magnified TEM bright-field image showing thin α_2-Ti_3Al plates in γ-TiAl. The SAED pattern inset shows rows of γ and α_2 diffraction spots. These rows are in the $[11\bar{1}]_\gamma$ direction (arrow). The grain surface orientation is (123)

solids, the annealed microstructures shown in Figs. 26 to 28 exhibit somewhat limited α_2 (Ti_3Al) coincident phase. This is particularly evident on comparing the SAED patterns in Figs. 20 and 21 with Fig. 28. The reduced α_2-phase is also evident from the corresponding XRD spectra as represented for the vertical reference planes for the two anneal schedules as shown in Fig. 29. The α_2 (002) and (201) peaks prominent in the 1150 °C anneal (top in Fig. 29) are absent in the 1380 °C anneal (bottom in Fig. 29). The α_2 (200) peak is small but unchanged for the two anneals. This is somewhat consistent with the TEM results shown in Figs. 27 and 28, respectively. Taken together, Figs. 26(b), 28, and the bottom XRD spectra in Fig. 29 are indicative of a lack of α_2 (Ti_3Al) phase. TEM bright- and DF analyses for the 1380 °C anneal samples indicated a significant fraction of the lamellar "plates" to be γ-twins. This is illustrated typically in the bright-field/DF TEM images represented in Fig. 30, where the grain surface orientation is (122), and the operating reflection for the twins coincided with the $(02\bar{2})$ diffraction spot. The average "lamellar" plate spacing was measured to be $\sim$0.9 μm from TEM images. This is also the twin width as illustrated in the DF image inset in Fig. 30. Twin planes along $[41\bar{3}]$ in Fig. 30 are coincident with $(1\bar{1}1)$ planes, inclined $\sim$79° to the (122) grain surface plane.

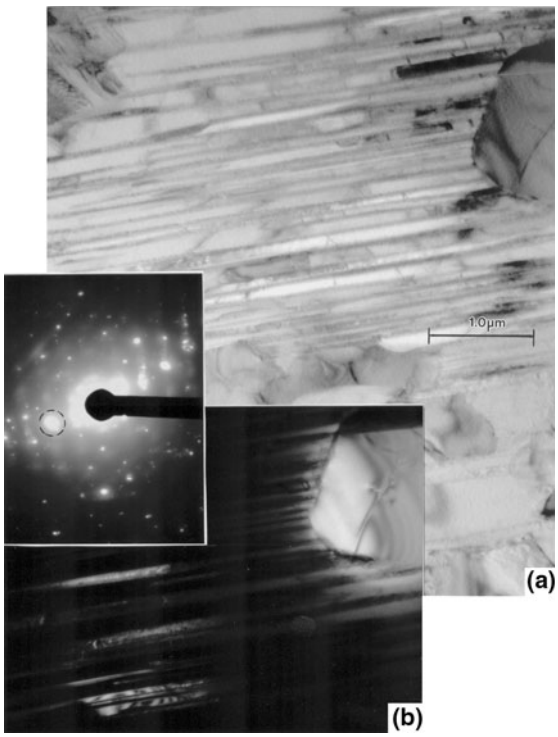

Fig. 21 TEM bright-field (**a**)/DF (**b**) sequence for α_2/γ lamellar microstructure. The DF image in (**b**) utilized the apertured γ diffraction spot shown circled in the SAED pattern inset. Only a small fraction of the γ-phase regions are imaged

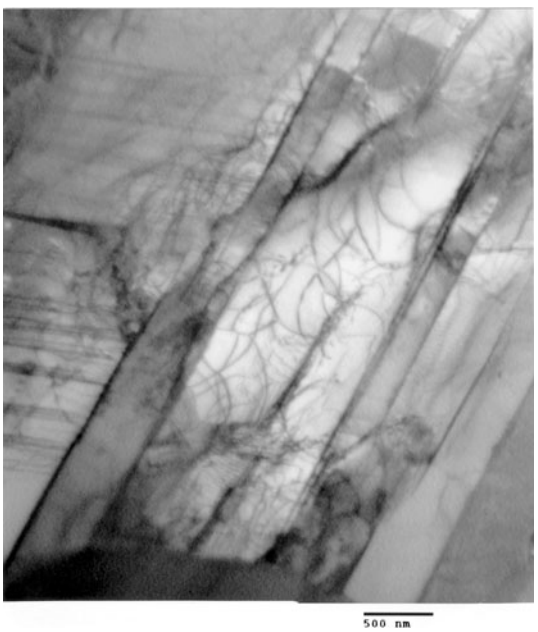

Fig. 22 TEM bright-field image for dislocation and lamellar microstructures observed in the horizontal reference plane for an EBM-fabricated cylindrical component (Fig. 2)

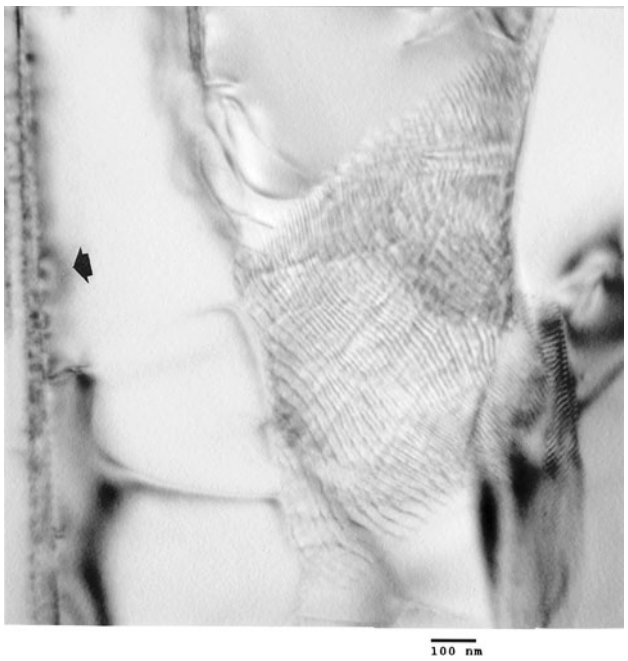

Fig. 23 TEM image showing large area composed of dislocation dipoles in a sample similar to Fig. 22. The α_2 lamellae at the extreme left of the micrograph exhibit strain-field contrast features (arrow) which may arise from interfacial steps or ledges

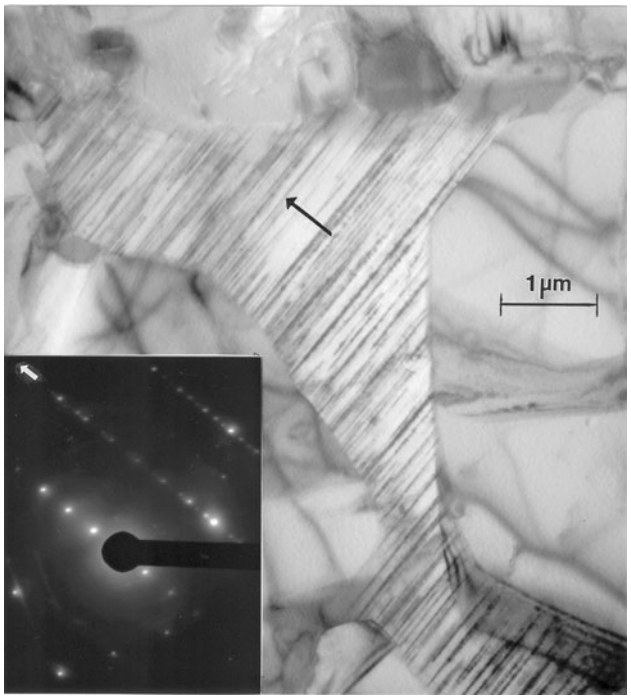

Fig. 24 TEM showing lamellar microstructures in the vertical reference plane for an EBM-fabricated cylindrical component. The SAED pattern inset is the same as that in Fig. 20. The arrows (black in the image and white in the SAED pattern) represent the $[11\bar{1}]_\gamma$ direction. The surface orientation is (123)

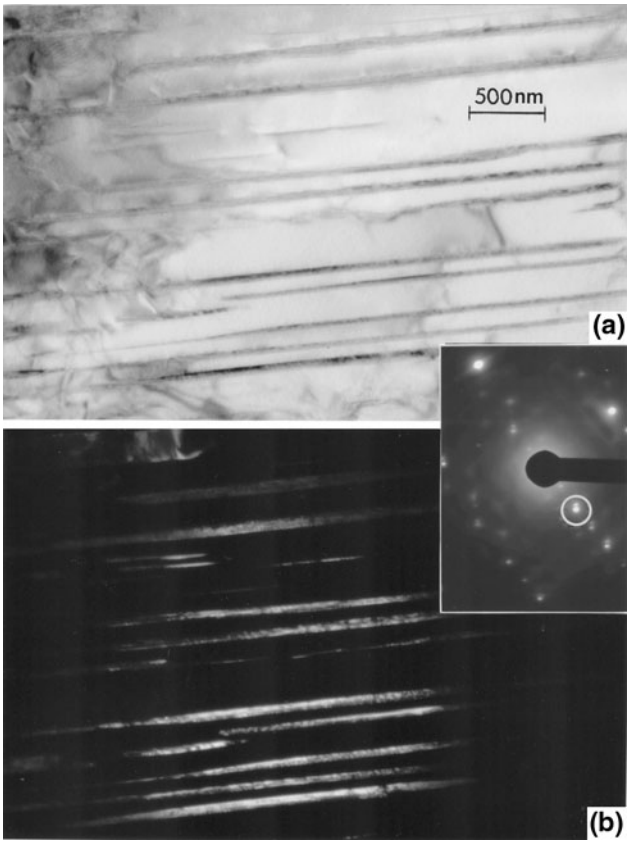

Fig. 25 Bright-field (**a**)/DF (**b**) TEM image sequence of α_2/γ lamellar microstructure in an EBM-fabricated cylindrical component (in the vertical reference plane). The DF image in (**b**) corresponds to the circled α_2 diffraction spot in the SAED pattern inset. The DF images in (**b**) represent portions of α_2 plates

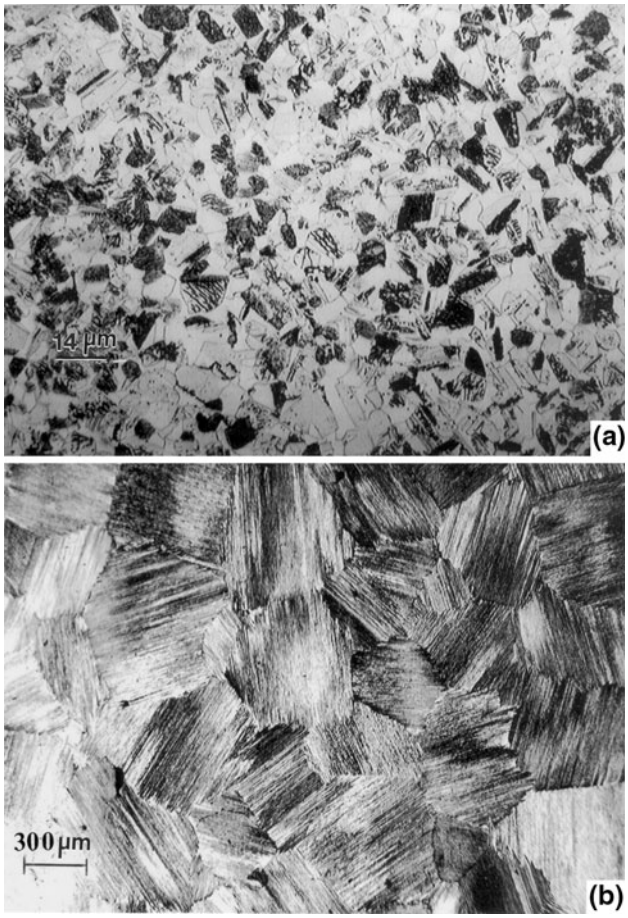

Fig. 26 LOM views for annealed EBM-built blocks in the vertical reference plane (parallel to the build direction. (**a**) Anneal (1): 1150 °C at 5 h. (**b**) Anneal (2): 1380 °C at 1 h

Discussion

Figure 26, in retrospect, represents a primarily γ-twinned (coherent {111} boundaries) microstructure with twins (and some coincident α_2-Ti_3Al phase platelets) forming a singular crystallographic ({111}) lamellar microstructure in the large, equiaxed grains. While the mechanism of twin formation is not fully understood, γ-twin boundary energies are certainly a fraction of the grain boundary energies, and their formation during anneal (at 1380 °C), from a simple thermodynamic point of view, is consistent with a reduction in the total free energy; especially the interfacial free energy contribution [18]. This energy reduction is further optimized by the growth of twin lamellae and the elimination of the coincident α_2 (Ti_3Al) phase.

The lamellar γ-TiAl twin structures which dominate the 1380 °C anneal (Fig. 26b) are reminiscent of nanoscale growth twin lamellae observed by Lu et al. [19] in nanograined copper synthesized using a pulsed electrodeposition technique which allowed for the nano-twin spacings to be varied from $\sim$100 to $\sim$ 15 nm, and dramatically enhancing mechanical properties (as much as a ten-fold increase in tensile strength in contrast to commercial, bulk copper) [20]. It is intriguing to speculate about the prospects for producing much smaller lamellar twin spacings in EBM-fabricated and selectively annealed γ-TiAl to enhance mechanical properties in a similar fashion, but not necessarily at the low-nanoscale.

Some indication of prospects for manipulating the mechanical properties for EBM-fabricated γ-TiAl products is provided in Fig. 31 which compares the Vickers microindentation hardness (HV) and the Rockwell C-scale (macroindentation) hardness (HRC) for the variety of EBM-fabricated products in this research program. Considering first the HV values [averaged in the horizontal and vertical reference planes for the solid block and cylindrical components and the block anneal schedules (Anneal 1 and 2)], there is a significant increment between the precursor (pre-alloyed) γ-TiAl powder and the foam ligaments. This is an indication of the α_2 (Ti_3Al) hardness representing a micro-dendritic structure in contrast to an equiaxed, α_2/γ grain structure in the foam ligaments. Correspondingly, the

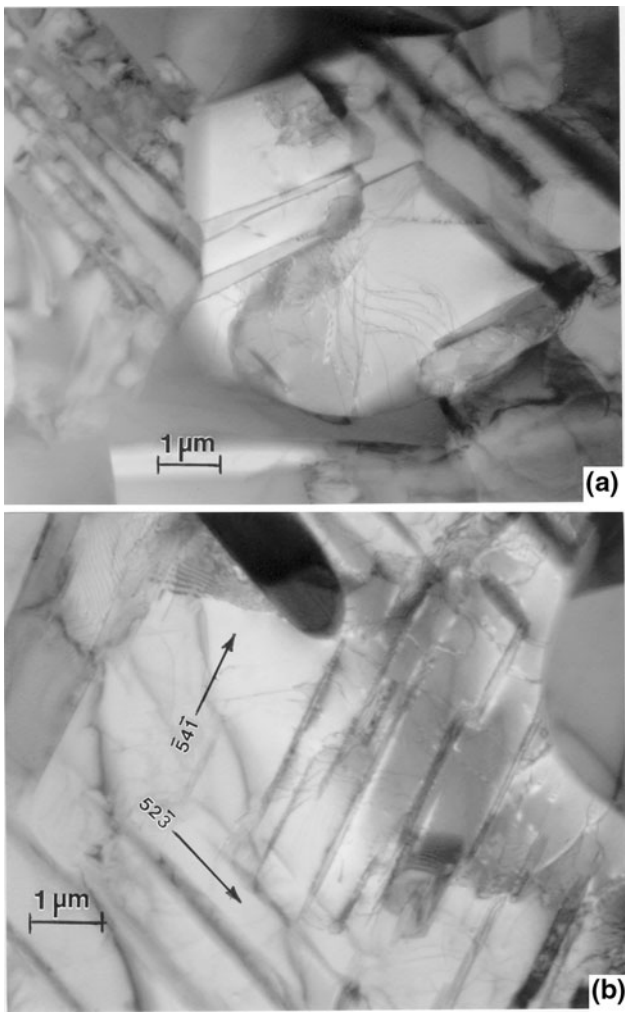

Fig. 27 Bright-field TEM images representing Anneal (1) (1150 °C at 5 h); corresponding to the LOM image in Fig. 26(a). (**a**) Mixture of fine α_2 and γ-twins. (**b**) Similar features for a larger grain with a (123) surface orientation. Corresponding γ-{111} trace directions are noted

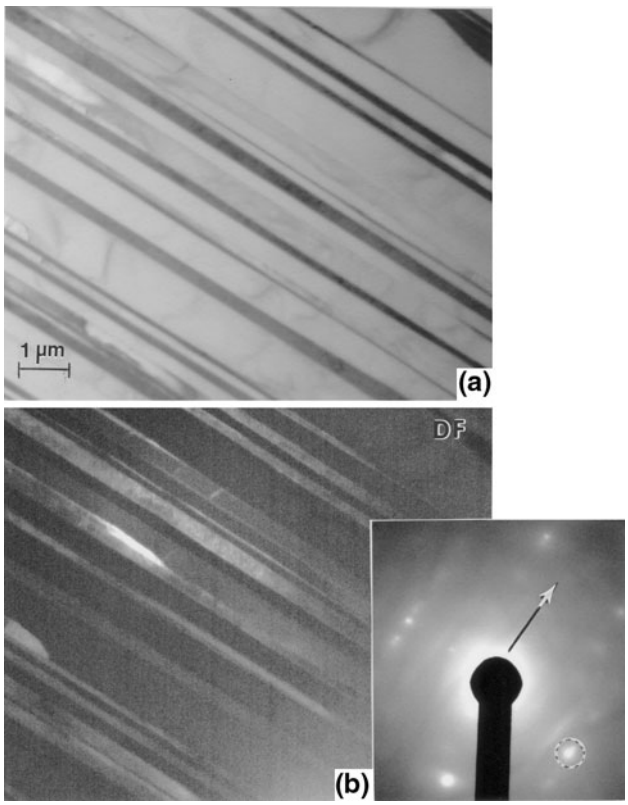

Fig. 28 TEM bright-field (**a**)/DF (**b**) image sequence utilizing the combined α_2/γ diffraction spots shown circled in the SAED pattern inset in (**b**). The TEM image sequence corresponds to Anneal (2) (1380 °C at 1 h) in the vertical reference plane, characteristic of the LOM image in Fig. 26(b). The arrow in the SAED pattern inset corresponds to $[11\bar{1}]$ for a (123) grain surface orientation

HV averages for all the solid components (including the annealed block) vary only by a few percent. This is particularly notable on comparing the EBM-fabricate block [with an equiaxed grain size of ~15 μm (containing) lamellar α_2/γ spaced ~100 nm with the 1380 °C anneal (Anneal 2)] where the equiaxed grain size was 550 μm with a "lamellar" spacing of ~0.9 μm. Correspondingly, the HV average increased slightly from 4.3 to 4.5 GPa. In contrast, the HRC averages (Fig. 31) declined for the EBM-fabricated block when annealed at 1380 °C: from HRC 42 to HRC 35, a 17% decrease. This is probably due primarily to the increased grain size for the 1380 °C anneal (Anneal 2). Certainly, optimizing the anneal schedule to reduce the grain size while simultaneously reducing the lamellar twin (or α_2-phase) thickness (and spacing) could raise the strength significantly. This prospect for interfacial microstructural engineering could lead to significant advances for γ-TiAl applications for components fabricated by EBM, especially prospects for annealed foam components as illustrated in Fig. 14.

In this context, it is interesting to note that the specific yield strength for γ-TiAl has been shown to be a maximum of ~150 MPa/g/cm^3 [1]. However, assuming as a simple rule-of-thumb that the yield strength is equal to one-third of the Vickers microindentation hardness [18], the solid EBM-fabricated components exhibit a specific strength of 312 MPa/g/cm^3 while the lowest density foam (Fig. 14) would have a corresponding specific strength of 3333 MPa/g/cm^3 (with reference to Fig. 31). This foam strength corresponds to an ideal specific yield strength nearly 200 times the conventional γ-TiAl specific strength [1].

Summary and Conclusions

EBM fabrication of rectangular, solid blocks, and cylinders (with nominal density of 3.85 g/cm^3) from pre-alloyed (Ti-48Al-2Cr-2Nb) powders has been examined by LOM and TEM. The microstructures exhibit a generally equiaxed, γ-

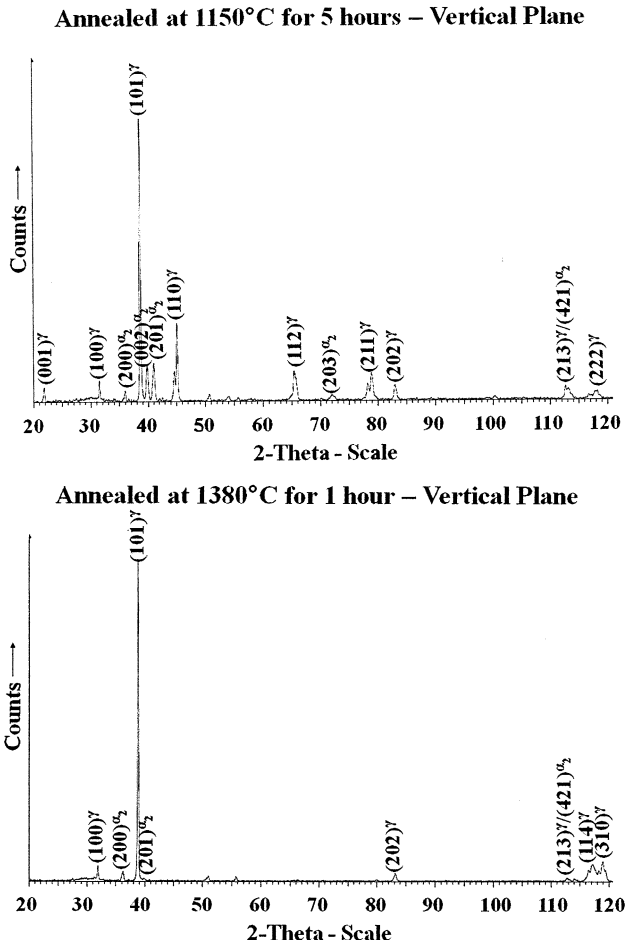

Fig. 29 XRD spectra corresponding to the vertical reference planes represented in Fig. 26(a) and (b), respectively

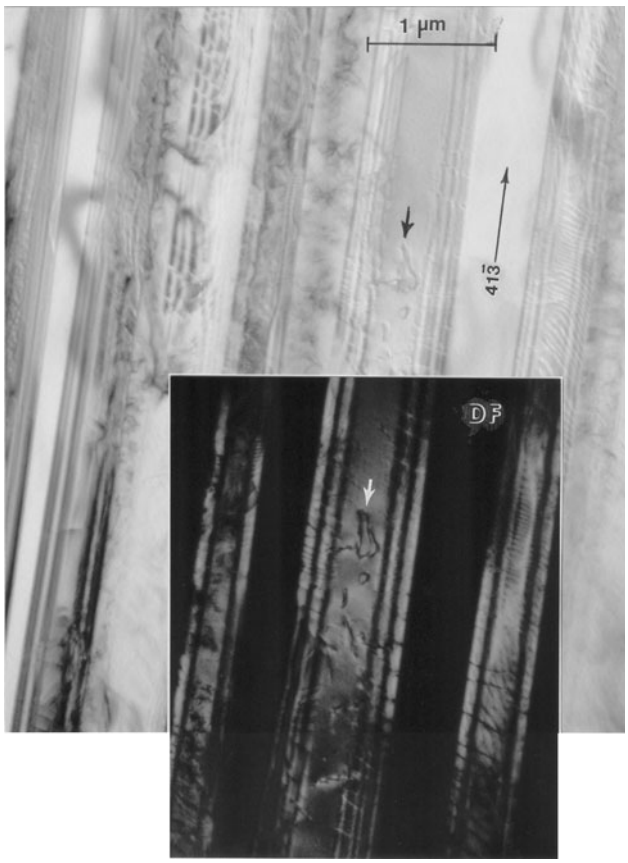

Fig. 30 TEM bright-field image for γ-twins coincident with (111) in a γ-TiAl (122) grain surface orientation. A DF image portion is inserted and corresponds to the twinned regions referenced by the arrow(s)

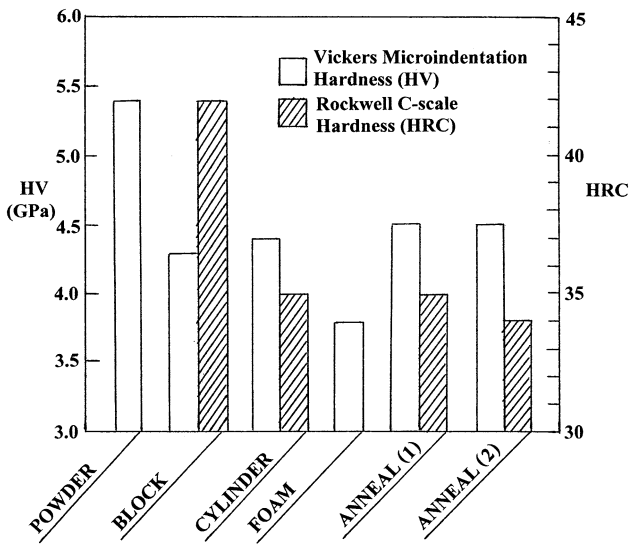

Fig. 31 Comparison of Vickers microindentation hardness averages (HV) and Rockwell C-scale hardness averages (HRC) for experimental specimens noted. The block, cylinder, Anneal (1), and Anneal (2) specimens averaged measurements made in the horizontal and vertical reference planes

TiAl grain structure with α_2/γ colonies exhibiting lamellar α_2/γ platelets. Grain sizes averaged $\sim$15 μm. This is in contrast to interdendritic spacings for mostly α_2 (Ti_3Al) in the precursor powder of $\sim$2 μm. XRD spectra for the solid components allowed α_2/γ to be estimated as 0.05 in contrast to $\sim$0.5 for the precursor powder. Prototype foam components, ranging in density from 0.33 to 0.46 g/cm^3 exhibited a ligament grain structure/duplex microstructure essentially the same as the solid components; including $\alpha_2/\gamma \cong 0.05$.

TEM bright- and DF sequences for the solid block and cylinder EBM fabricated components confirmed the α_2/γ lamellar, duplex microstructures to be the same as those characterized earlier for more conventionally processed γ-TiAl: investment casting and powder metallurgy-produced ingots. This included the $(111)_\gamma \| (0001)\alpha_2$ orientation relationship.

Simple anneal schedules for the solid block EBM fabricated components included 1150 °C at 5 h and 1380 °C at 1 h. These produced a fine, equiaxed duplex grain

structure ($\sim$3 μm) with $\alpha_2/\gamma < 0.05$, and a very large, equiaxed grain structure ($\sim$550 μm) with a fully lamellar microstructure, respectively. TEM bright- and DF image sequencing along with XRD spectral data indicated that $\alpha_2/\gamma \ll 0.05$, and the lamellar structure to be mostly coherent {111} γ-TiAl twins. This lamellar twin structure averaged twin widths and spacings of $\sim$0.9 μm in contrast to lamellar α_2 (Ti_3Al) widths of $\sim$20 nm and spacings of $\sim$0.1 μm in the as-fabricated components.

Both annealed components (1150 and 1380 °C) exhibited Vickers microindentation hardnesses similar to the EBM-fabricated components, suggesting that optimizing the grain size and reducing the lamellar coherent twin spacings through selective annealing could allow for superior mechanical properties for a range of applications of EBM-fabricated γ-TiAl products.

Acknowledgments We are grateful to Dave Abbott of GE for the provision of the pre-alloyed TiAl powder. This research was supported in part by a Mr. and Mrs. MacIntosh Murchison Endowment at the University of Texas at El Paso.

References

1. F. Appel, R. Wagner, Microstructure and deformation of two-phase γ-titanium aluminides. Mater. Sci. Eng. **R22**, 187–268 (1998)
2. F. Appel, U. Brossmann, U. Christoph, S. Eggert, P. Janschek, U. Lorenz, J. Müllar, M. Oehring, J.D.H. Paul, Recent progress in the development of gamma titanium aluminide alloys. Adv. Eng. Mater. **2**(11), 699–720 (2000)
3. H. Zhu, D.Y. Seo, K. Maruyama, Strengthening behavior of beta phase in lamellar microstructure of TiAl alloys. J. Manag. **62**(1), 64–69 (2010)
4. T.E. O'Connell, J.A. Miller, *Interior Technical Report AFML-TR-78-129* (WPAFB, Dayton, 1978)
5. F.H. Froes, C. Suryanarayana, D. Eliezer, Synthesis, properties and applications of titanium alumines (review). J. Mater. Sci. **27**, 5113–5140 (1992)
6. D. Cormier, O.L. Harryson, T. Mahale, H. West, Free form fabrication of titanium aluminide via electron beam melting using prealloyed and blended powders. Res. Lett. Mater. Sci. **2007**, article Ib34737 (2007)
7. L.E. Murr, S.M. Gaytan, A. Ceylan, E. Martinez, J.L. Martinez, D.H. Hernandez, B.I. Machado, D.A. Ramirez, F. Medina, S. Collins, R.B. Wicker, Characterization of titanium aluminide alloy components fabricated by additive manufacturing using electron beam melting. Acta Mater. **58**, 1887–1894 (2010)
8. H. Inui, M.H. Oh, A. Nakamura, M. Yamagushi, Ordered domains in TiAl coexisting with Ti_3Al in the lamellar structure of Ti-rich TiAl compounds. Philos. Mag. **A66**, 539–555 (1992)
9. M. Barnabes, P. Sevilla, J.A. Planell, F.J Gill, Mechanical properties of nickel-titanium foams for reconstructive orthopedics. Mater. Sci. Eng. **28**(1), 23-27 (2008)
10. A.M. Hodge, D.C. Dunand, Modeling of creep in open-cell NiAl foams. Metall. Mater. Trans. A **34**, 2352–2361 (2003)
11. L.E. Murr, S.M. Gaytan, F. Medina, H. Lopez, E. Martinez, D.H. Hernandez, M.I. Lopez, R.B. Wicker, J. Bracke, Next generation biomedical implants using additive manufacturing of complex cellular and functional mesh arrays. Philos. Trans. R. Soc. A **368**, 1999–2032 (2010)
12. L.E. Murr, S.J. Li, Y.-X. Tian, K. Amato, E. Martinez, F. Medina, Open-cellular Co-base and Ni-base superalloys fabricated by electron beam melting. Materials **4**, 782–790 (2011)
13. C. Koeppe, A. Bartels, J. Seeger, H. Mecking, General aspects of the thermomechanical treatment of two-phase intermetallic TiAl compounds. Metall. Trans. **24A**, 1795–1802 (1993)
14. Y.-W. Kim, R. Wagner, M. Yamaguchi (eds.), *Gamma Titanium Aluminides* (TMS, Warrendale, 1995)
15. R. Wagner, F. Appel, B. Dugan, R.J. Eniss, U. Lorenz, J. Mullauer, H.P. Nicolai, W. Quadakkers, L. Singheiser, W. Smarsly, W. Vaidya, K. Wurzwallner, in *Gamma Titanium Aluminides*, ed. by Y.-W. Kim, R. Wagner, M. Yamaguchi (TMS, Warrendale, 1975), p. 387
16. B. London, *Structural Intermetallics* (TMS, Warrendale, 1993), p. 151
17. Y.-W. Kim, Ordered intermetallic alloys: part III: gamma titanium aluminides. J. Manag. **46**, 30–35 (1994)
18. L.E. Murr, *Interfacial Phenomena in Metals and Alloys* (Addison-Wesley, Reading, 1975) (reprinted in 1990 and available from CRBL.com)
19. L. Lu, Y.-F. Shen, Xr.H. Chen, L. Qian, K. Lu, Ultrahigh strength and high electrical conductivity in copper. Science **304**, 422–426 (2005)
20. K. Lu, L. Lu, S. Suresh, Strengthening materials, by engineering coherent internal boundaries at the nanoscale. Science **324**, 349–352 (2009)